Editors' Suggestion

Anomalous electronic energy relaxation and soft phonons in the Dirac semimetal Cd_3As_2

Rishi Bhandia,[1,*,†] David Barbalas,[1,*] Run Xiao,[2,1] Juan R. Chamorro,[3,1] Tanya Berry,[3,1] Tyrel M. McQueen,[1,3,4] Nitin Samarth,[1,2,5] and N. P. Armitage[1,‡]

[1]*The Institute of Quantum Matter, Department of Physics and Astronomy, The Johns Hopkins University, Baltimore, Maryland 21218, USA*
[2]*Department of Physics, The Pennsylvania State University, University Park, Pennsylvania 16802, USA*
[3]*Department of Chemistry, Johns Hopkins University, Baltimore, Maryland 21218, USA*
[4]*Department of Materials Science and Engineering, The Johns Hopkins University, Baltimore, Maryland 21218, USA*
[5]*Department of Materials Science and Engineering, The Pennsylvania State University, University Park, Pennsylvania 16802, USA*

(Received 6 May 2024; revised 24 June 2024; accepted 24 July 2024; published 15 August 2024)

We have used a combination of linear response time-domain THz spectroscopy (TDTS) and nonlinear THz pump-probe spectroscopy to separately probe the electronic momentum and energy relaxation rates, respectively, of the Dirac semimetal Cd_3As_2. We find, consistent with prior measurements, that Cd_3As_2 has enormous nonlinearities in the THz frequency range. We extract the momentum relaxation rate of Cd_3As_2 using Drude fits to the optical conductivity. We also conduct THz-range 2D coherent spectroscopy and find that the dominant response is a pump-probe signal, which allows us to extract the energy relaxation rate. We find that the rate of energy relaxation decreases down to the lowest measured temperatures. We connect this to Cd_3As_2's anomalous lattice dynamics, evidence for which is found in its low thermal conductivity and soft phonons in Raman scattering. We believe the lack of a peak in the energy relaxation rate as a function of T is related to the linear-in-T dependence of the current relaxation at low T; e.g., the phonon scattering is elastic from the lowest measured temperature, 5 K, to at least as high as 120 K.

DOI: 10.1103/PhysRevB.110.075131

I. INTRODUCTION

In the past 20 years, a significant theme in condensed matter physics has been the identification, characterization, and study of a range of materials that possess low-energy excitations well-described by massless Dirac fermions. As a consequence of this unusual low-energy excitation spectrum, these systems exhibit unique properties in their electronic transport or optical response [1–4]. Although many of these systems are inherently two-dimensional, Weyl or Dirac semimetals are a class of three-dimensional materials that host linear band touchings in momentum space [5]. These features allow for the exploration of novel materials physics arising from these conditions. Unlike graphene, the three-dimensional nature of topological semimetals allows for the enhancement of light-matter interactions due to their finite thickness, leading to many predictions for their applications in high-speed electronic, optoelectronic, and spintronic devices [6–10].

$Cd_3As_2$is an archetypal example of a Dirac semimetal [11–13]. In contrast to other Dirac semimetal candidates, such as Na_3Bi, Cd_3As_2 is stable under ambient conditions, making it ideal for applications in devices. It has an almost cubic symmetry with a lattice superstructure associated with Cd vacancies, which greatly enlarges the unit cell to 80 atoms, but preserves inversion and time-reversal symmetry [14]. These symmetries allow for fourfold degenerate Dirac points. Calculations and photoemission experiments anticipate and find two Dirac points located near the Γ point, along the $\Gamma - Z$ direction [11].

Before its recognition as a Dirac semimetal, Cd_3As_2 had already drawn attention for its exceptional mobility, initially observed in 1959 [15]. Recent transport measurements have revealed phenomena like giant magnetoresistance, quantum oscillations, and the quantum Hall effect (QHE) in Cd_3As_2, alongside observations of the chiral anomaly [16–25].

The lattice properties of Cd_3As_2 are also anomalous. It has one of the lowest lattice thermal conductivities ever measured at room temperature, 0.3 to 0.7 $W\,m^{-1}\,K^{-1}$ [26–29]. Crystalline materials with similar atomic masses and structures typically have a lattice thermal conductivity 1–3 orders of magnitude larger [26]. This low thermal conductivity is believed to arise as a consequence of the large unit cell that gives rise to a large number of optical phonons that depress the acoustic phonon velocity and mean free path. Moreover, an anomalous low temperature softening of a group of zone center Raman active phonons has been found [27]. It has been proposed that these soft modes and low frequency optical phonons increase the phase space for scattering of the heat-carrying acoustic phonons and are—in part—the origin of the low lattice thermal conductivity of Cd_3As_2 [27]. Despite these observations, little progress has been made in understanding the interplay between Cd_3As_2's unusual electronic and lattice dynamics. Among other aspects, it is essential to understand these effects as they can influence device characteristics under nonequilibrium hot-electron conditions in various ways.

*These authors contributed equally.
†Contact author: rbhandia@jhu.edu
‡Contact author: npa@jhu.edu

One method of studying the coupling between electronic and lattice degrees of freedom is nonlinear (terahertz) THz pump-probe experiments [30–32]. Pump-probe experiments can measure the rate that energy leaves the electronic system via coupling to some external bath [33–35]. This is in contrast to the momentum (or more strictly speaking the current) relaxation rate that is usually measured in conventional transport and optical experiments. However, most ultrafast pump-probe experiments have utilized near-infrared or optical frequency (1 to 3 eV) pump sources, which drive the electronic and lattice subsystems into regimes very far from equilibrium [36–43]. With such high energy excitations, the usual quasiequilibrium approximations may be invalid, as the energy scales initially excited are many orders of magnitude higher than the energy scales relevant to the low-temperature phenomena of solids. Hence, interpretation usually rests on the assumption of very fast relaxation to a quasithermal distribution that is subsequently probed. In contrast, THz-range nonlinear spectroscopy is an attractive tool to probe couplings in the low-energy scale (meV) regime.

In this paper, we perform both conventional linear time-domain THz spectroscopy and nonlinear THz pump-probe on films of Cd_3As_2 to separately measure the momentum and energy relaxation rates. Via conventional linear response time-domain spectroscopy, we observe that the momentum relaxation rate is weakly dependent on temperature up to 300 K. Utilizing nonlinear THz measurements, we build on previous studies observing large THz third-harmonic generation in Cd_3As_2, as we measure the temperature-dependent, third-order nonlinear susceptibility $\chi^{(3)}(\omega)$ over the THz frequency range [44,45]. This allows us to more clearly understand dominant nonlinear processes of Cd_3As_2 while elucidating the nature of electron-phonon dynamics via careful examination of pump-probe processes and energy loss from the electron system. We find that the rate of energy loss from the electronic system decreases as temperature increases from our lowest to highest measured temperatures. This is at odds with expectation where a peak in the energy relaxation rate is expected at temperature set by the Bloch-Grüneisen temperature [46]. We connect this surprising behavior to the anomalous phonon dynamics of Cd_3As_2, as evidenced by its low thermal conductivity and the observation of soft phonons in Raman scattering [27,29,47,48]. We believe the lack of a peak in the energy relaxation rate as a function of T can be connected to the linear-in-T dependence of the current relaxation, e.g., the phonon scattering is dominantly elastic down to the lowest measured temperatures. Both thermal conductivity and electrical resistivity are then dominated by the same scattering mechanisms and one expects that the Wiedemann–Franz law would then be satisfied for Cd_3As_2 over this large range of temperatures [49].

II. EXPERIMENTAL DETAILS

The 100 nm $Cd_3As_2(112)$ thin films were grown via molecular beam epitaxy on (111) GaAs substrates with a 100 nm GaSb buffer layer. These films were monitored during the growth process with reflection high-energy electron diffraction to assess the surface quality. See earlier work for more detail on the growth process [24]. Prior angle-resolved photoemission spectroscopy (ARPES) on thin films grown under these conditions has confirmed the presence of Dirac cones while x-ray diffraction has confirmed presence of peaks corresponding to the $Cd_3As_2(112)$ planes [50].

We performed conventional linear response THz measurements on these samples utilizing our custom time-domain THz spectrometer coupled to a helium vapor flow cryostat. The THz pulses were generated using a fiber oscillator laser (Toptica Femtofiber smart 780) that produced a 780 nm, 120 fs pulses at a repetition rate of 80 MHz. These pulses are split into two beams. One was used to generate a THz pulse using a voltage-biased photoconductive antenna (PCA), while the other beam was used to gate an unbiased PCA to detect the THz pulse. By measuring the transmitted THz pulse through the sample and an appropriate substrate reference, we can calculate the complex transmission coefficient. Then, by inverting the equation $T(\omega) = \frac{1+n_{\text{sub}}}{1+n_{\text{sub}}+Z_0 d\sigma(\omega)} \exp[i\frac{\omega}{c}(n_{\text{sub}} - 1)\Delta L]$ we can obtain the complex conductivity $\sigma(\omega)$ of the film. Here $T(\omega)$ is the measured complex transmittance of the thin film, n_{sub} the index of refraction of the substrate, d the thin film thickness, and ΔL the factor to account for differences in thicknesses between substrate and sample.

For the nonlinear THz spectroscopy, we conducted experiments in a now standard THz 2D coherent spectroscopy geometry with two $LiNbO_3$ THz sources as described elsewhere [30,51,52]. At its maximum, the incident field strength was 40 kV cm^{-1} per pulse with a center frequency of 0.6 THz. To measure the nonlinear response, we used a differential chopping scheme that allowed us to measure the transmitted pulses E_A and E_B separately, and then pulses E_{AB} transmitted together. From this, we can calculate the nonlinear response via subtraction, $E_{\text{NL}} = E_{AB} - E_A - E_B$. We sample the response in time, t, and control the delay between the pulses, τ, with a pair of delay stages. The incident electric field strength is controlled with a pair of wire-grid polarizers. If the THz pulse energy is absorbed entirely into the electronic system and can be considered to go entirely into a thermal distribution, the heating at room temperature (300 K) of the electronic subsystem is negligible, but can become significant at low temperatures. We elaborate on the impact of this heating on the interpretation of our pump-probe experiments further below.

III. ANALYSIS AND RESULTS

The complex optical conductivity measured at different temperatures for a representative thin film is shown in Fig. 1(a). One sees a large Drude-like peak that arises from free-charge carrier motion. At lower temperatures, a very small 0.6 THz optical phonon feature that was resolved in previous studies becomes apparent [53]. The temperature-dependent conductivity is roughly what we expect for a high mobility semimetal. A larger width indicates increased carrier scattering at high temperature. The increased area and overall scale of the conductivity curves indicates slightly larger plasma frequency at higher temperatures. We can fit the optical conductivity to the standard expression for the Drude

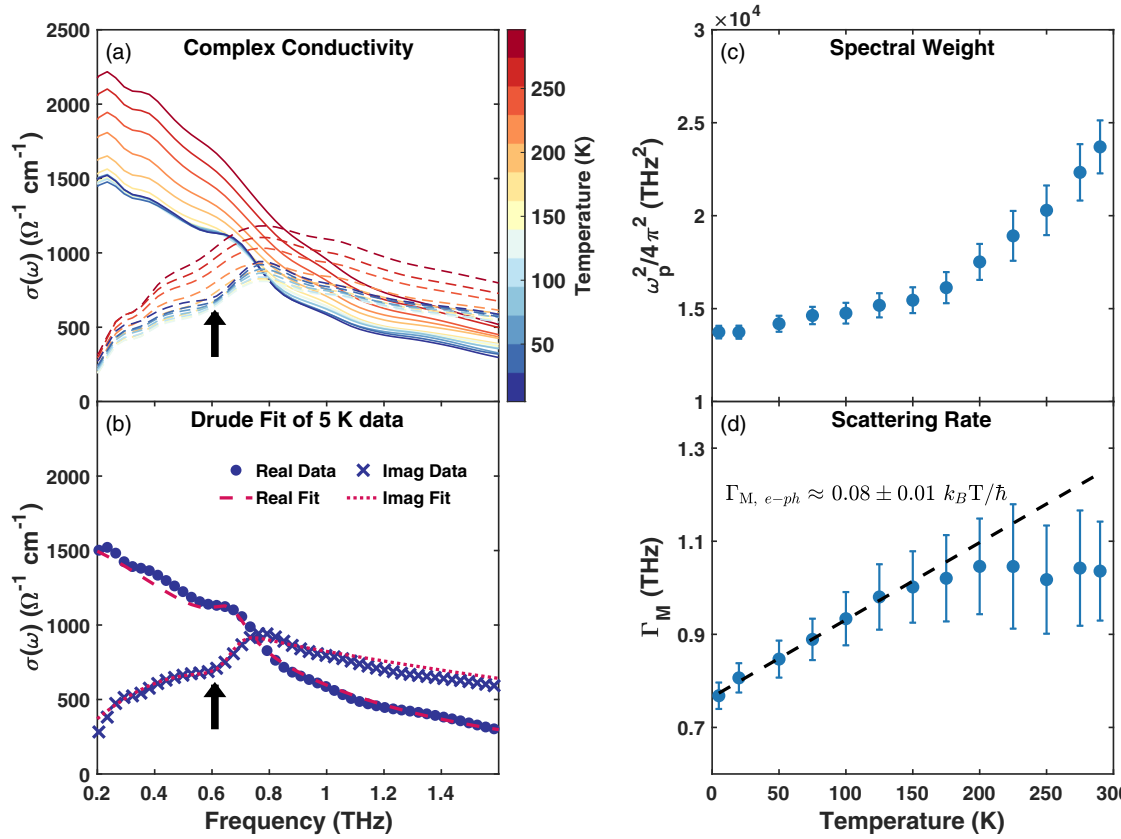

FIG. 1. (a) THz complex conductivity of a 100 nm thin film of Cd_3As_2. The real (imaginary) optical conductivity is plotted as solid (dashed) lines for temperatures from 5 to 290 K. The arrow indicates a feature in the conductivity corresponding to an optical phonon. (b) An example fit (markers) to the model described in the text (dashed lines). (c) The fitted spectral weight of the electronic Drude term. (d) The scattering rate, Γ_M, obtained from the Drude fits. Dotted line is a linear fit emphasizing the linear-in-T dependence from 5 K to 120 K, corresponding to elastic scattering from phonons. From this fit, we can estimate the electron-phonon contribution to the scattering rate as $0.08 \pm 0.01\ k_B T/h$.

model with another term for the optical phonon

$$\sigma(\omega) = \epsilon_0 \left[\frac{-\omega_p^2}{i\omega - 2\pi\Gamma_M} - i(\epsilon_\infty - 1)\omega \right] + \sigma_{\text{ph}}(\omega), \qquad (1)$$

where ω_p is the Drude plasma frequency, Γ_M is the current relaxation rate, and ϵ_∞ is the high frequency dielectric constant, which accounts for the effects of higher band interband transitions on the low frequency dielectric constant. σ_{ph} is a Fano-shaped Lorentz oscillator that accounts for the screened optical phonon that appears at lower temperatures near 0.6 THz [54,55]. Figure 1(b) shows an example fit. This phonon had been seen in previous studies [53], but appears much weaker here due to the larger carrier density of these films and attendant screening effects. The results of these fits are shown in Figs. 1(c) and 1(d). The scattering rate, Γ_M, is plotted as a function of temperature in Fig. 1(d). Formally, this rate is the current or transport relaxation rate [49]. For materials with sufficiently isotropic dispersion, it is equivalent to the momentum relaxation rate. As one would expect, this rate increases with increasing temperature in all the Cd_3As_2 films measured, however, its explicit dependence can be noted as anomalous. One expects the electron-phonon interaction to give a low-temperature scattering rate that goes as T^3–T^5 depending on the degree to which large angle scattering is important. We instead observe that $\Gamma_m \propto T$ up to ∼120 K, as shown in Fig. 1(d), above which the T dependence gets weaker.

As the plasma frequency (ω_p) varies inversely with the effective mass, we can attribute the plasma frequency's measured temperature dependence to the temperature dependence of the effective mass. Since $\omega_p \propto E_F$ for electrons with linear dispersion in three dimensions, when comparing to prior measurements of the plasma frequency in magento-optic experiments [53], we can estimate the Fermi energy to be ∼0.2 eV above the Dirac point. This is consistent with the Fermi energy measured via ARPES in Cd_3As_2 thin films grown under similar conditions [50]. It is interesting to note the approximately T^2 dependence of the plasma frequency (with an offset) is similar to what is predicted for linearly dispersing systems in general [56]. However, note that Cd_3As_2 does have large parabolic contributions to its dispersion only 10s of meV away from its Dirac points, so any close comparisons would have to take into account details of the band structure [17].

To determine the overall scale of the nonlinear response, we first conducted experiments where we set the time delay between the two pulses to $\tau = 0$ and then measured $E_{\text{NL}}(t, \tau = 0)$ as discussed above. In Fig. 2(a), we plot the time trace of the nonlinear response at different temperatures. Here the plotted electric field is the electric field strength at the sample position. As shown, the nonlinear response increases

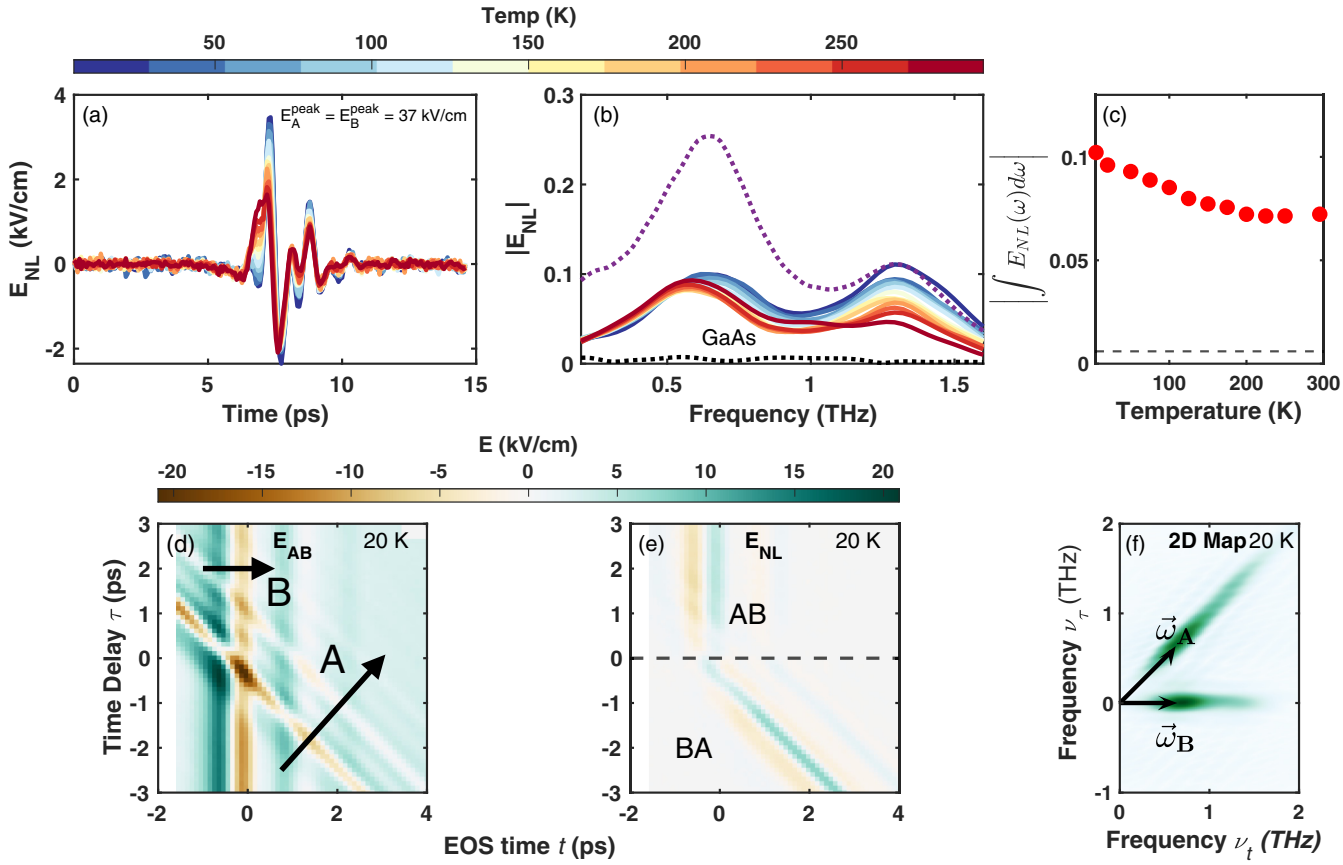

FIG. 2. The nonlinear THz spectra of the 100 nm Cd_3As_2 thin film. (a) Time trace of the nonlinear signal $E_{\rm NL}(t, \tau = 0)$ (b) The Fourier transform of the data in (a). The black dotted line is the $\tau = 0$ nonlinear response of the bare GaAs substrate. The purple dotted line is the input pulse spectrum divided by a factor of 7.5 to be made visible on the plot. (c) The nonlinear spectra from (b) integrated over the range 0.3 to 1.4 THz. The dotted black line gives the intensity of GaAs nonlinear spectrum integrated over the same frequency range. (d) Time traces of $E_{AB}(t, \tau)$. (e) The nonlinear component of (d), $E_{\rm NL}(t, \tau)$. (f) A 2D THz spectra of $|E(\nu_\tau, \nu_t))|$ obtained by taking at 2D FFT of $E_{\rm NL}(t, \tau)$. The only nonlinear process we observe is pump probe.

monotonically as we cool to lower temperatures. To confirm that the nonlinear response is intrinsic to the Cd_3As_2, we also measured the nonlinear response of GaAs as a function of temperature. In Fig. 2(b), the Fourier transform (FFT) of the nonlinear response is plotted at different temperatures. We observe that the nonlinear response of the sample is far larger than the nonlinear response of the substrate (thin dashed black line), confirming that the source of these optical nonlinearities is the Cd_3As_2 thin film. The purple dotted line is the input pulse, E_{AB}, divided by a factor of 5 to be made visible on the plot.

To identify the source of the nonlinear signal, we can construct a 2D coherent spectrum by sweeping the time delay between the two intense THz pulses and the electro-optic sampling time. The results are shown in Fig. 2(d). We plot the nonlinear component of the THz response in Fig. 2(e) and take a 2D FFT of it to obtain a 2D spectra as shown in Fig. 2(f). Here we have two different pump-probe contributions appearing as streaked peaks. The two separate peaks in the 2D plot correspond to the two different possible time orderings of the A and B pulses; the diagonal (horizontal) is where pulse B (pulse A) acts as the pump pulse and pulse A (pulse B) acts as the probe, known as the BA regime (AB regime). The position they appear in the 2D spectra can be understood according to frequency vectors $\vec{\omega}_{AB:PP} = \vec{\omega}_A - \vec{\omega}_A + \vec{\omega}_B = \vec{\omega}_B$ or $\vec{\omega}_{BA:PP} = \vec{\omega}_B - \vec{\omega}_B + \vec{\omega}_A = \vec{\omega}_A$ and hence follow from processes that go as $E_A^* E_A E_B$ and $E_B^* E_B E_A$ [51]. These are pump-probe contributions to the nonlinear response. As $E_A^* E_A$ and $E_B^* E_B$ are intensities, the dependence of the response as a function of the interpulse separation τ is a measure of how fast the system recovers from pump. Such nonlinear pump-probe processes are the expected dominant nonlinear process in metals [57].

In general, the pump-probe processes driving these nonlinearities can be understood as the THz pump (here E_A), creating a Fermi surface perturbation, which is then probed by E_B as it relaxes back to equilibrium. To get a very rough feeling for the size of these effects, we can consider heating due to the high-field THz pulses incident on the sample. As nonlinearities are, in general, small as compared to the linear effects, we make an estimate of the energy absorbed per unit volume by $Q = \int_0^T \sigma_1(0.6\,\text{THz})[E_A^{\text{inside}}(t)]^2 dt$, where T is the pulse length ($\sim$1 ps). We use $\sigma_1(0.6\,\text{THz})$ as an estimate of the relevant conductivity as it is the frequency of maximum THz field. E_A^{inside} can be estimated from E_A as discussed in the Supplemental Material of Ref. [58] to be at a maximum drive field of $\sim$7 to 9 kV/cm. As our measured THz

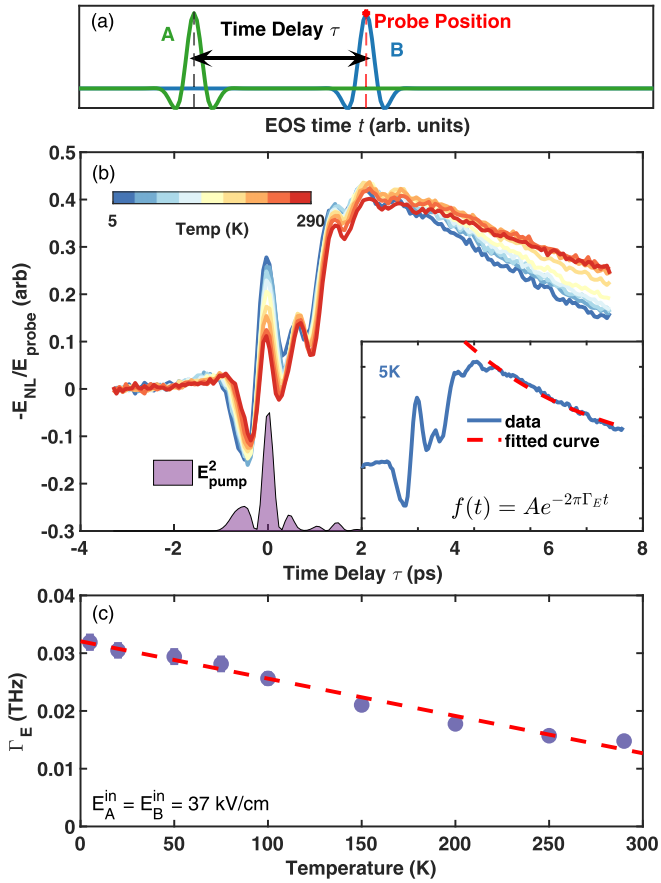

FIG. 3. Nonlinear THz pump-THz-probe time traces of a representative 100 nm Cd_3As_2 thin film. (a) A schematic of our experiment. (b) Pump-probe time traces as a function of temperature. Note that the decay rate changes visibly, with the slope becoming steeper at lower temperatures. The purple shaded area is the time profile of $E^2_{\text{pump}}(\tau)$ inside the sample in arbitrary units. $\int E^2_{\text{pump}}(\tau)d\tau \propto Q_{\text{film}}$, the heat energy deposited in the electronic subsystem. The inset is an example fit of a decay to extract the energy relaxation time. (c) Measured energy relaxation rates Γ_E as a function of temperature.

conductivity spectra is dominated by the intraband Drude term, the deposited energy goes into raising the temperature of a quasithermal electronic distribution. One can estimate the rise in effective temperature of the electrons (using the measured electronic contribution to the heat capacity of $C_e = \gamma T$ with $\gamma = 5.33\,\text{mJ}\,\text{mol}^{-1}\,\text{K}^{-1}$ [38,59]) as 58 K at 10 K and 5.8 K at 100 K. Hence, the perturbation is large at the lowest temperatures for the largest drive fields, but as we will note we see the same qualitative temperature dependencies for the lower drive fields that deposit only 1/10 as much energy.

A schematic of our pump-probe experiments is shown in Fig. 3(a). The probe time t is fixed as the time delay between the pulses, τ, is varied. Pump-probe time traces taken at different temperatures are shown in Fig. 3(b). We normalize the plotted nonlinear signal, E_{NL} by the probe field (E_B) to account for the temperature-dependent conductivity of the film. A factor of -1 is included to account for the fact the pump decreases the transient transmittance. For times after both pumps have arrived, one sees two distinctly different regions of behavior. At early times, there is interference between the A and B pulses. As one can see from Fig. 2(e), this comes from a region of order of the pulse duration (∼2 ps) around $\tau \sim -t$ where there is ambiguity about the time ordering of the pulses. This leads to oscillations in this time region that are due to the pump-probe processes, but from when B pulse comes before A. For times $\tau \gg -t$, the signal shows decaying behavior. As discussed in Ref. [30], after an E^2 perturbation the decay at long times is expected to be largely governed by the rate of energy relaxation e.g. the rate that energy leaves the electronic systems. By fitting to a model of exponential decay ($\propto e^{-2\pi\Gamma_E t}$) at times well after the pulse [as shown in Fig. 3(b)], we obtain the energy relaxation rate as shown in Fig. 3(c) at different temperatures. We find that Γ_E increases as temperature decreases over the whole measured temperature range [Fig. 3(c)]. This Γ_E is associated with energy leaving the electronic subsystem via coupling to nonoptically active degrees of freedom [60]. One generally expects the energy relaxation rate to be less than the momentum relaxation rate, as the latter is essentially a backscattering weighted average over all scattering processes, whereas Γ_E is only sensitive to a small minority of inelastic processes that remove energy from the electronic system. In a high mobility semimetal, we expect it to arise from mainly electron-acoustic phonon scattering. For low frequency phonons, it is expected that at higher temperatures they are excited to such a degree that they are as absorbed as often as they are emitted and are hence inefficient sinks of energy.

It is interesting to compare the observed rates to expectations. A derivation of energy relaxation rates by Allen [46] was based on a model of a Debye model for the acoustic phonons (with subsequent refinements [33,60]). In this two-temperature model, one considers the system after optical excitation as having electrons that quickly thermalize to a temperature T_e and then over longer timescales lose energy to the lattice that is at a lower temperature T_L. At temperatures well above the Bloch-Grüneisen scale, Γ_E is expected to have an increasing dependence with decreasing temperature that goes as

$$\Gamma_E = \frac{6\hbar\lambda\langle\omega^2\rangle}{k_B T_e}, \tag{2}$$

where T_e is the temperature of the electronic subsystem and $\lambda\langle\omega^2\rangle$ is the second moment of the Eliashberg function given by $\lambda\langle\omega^2\rangle = 2\int_0^\infty d\Omega[\alpha^2F(\Omega)/\Omega]\Omega^2$ [33,46,60] that quantifies the coupling to acoustic phonons. In a conventional metal, the Bloch-Grüneisen temperature is $T_{\text{BG}} = 2k_F v_s\hbar/k_B$ (where v_s is the speed of sound). As the temperature is lowered below $\sim 0.3T_{\text{BG}}$ [60], Γ_E starts to decrease and is expected to cross over to a dependence that goes as T_e^3 with a coefficient close to the expectation for the acoustic phonon contribution to the electron-hole two-particle self energy. The data is at odds with these simple expectations as Γ_E is an increasing function with decreasing T over the whole range.

In Figs. 4(a) and 4(b), we plot the energy relaxation rates as a function of field strength (normalized to the maximum field $40\,\text{kV}\,\text{cm}^{-1}$) at different temperatures and as a function of temperature at different fields. At room temperature, the relaxation times, 290 K, show no dependence on the pump electric field. However, at lower temperatures we see a dependence that shows enhanced decay rates at the lowest temperatures

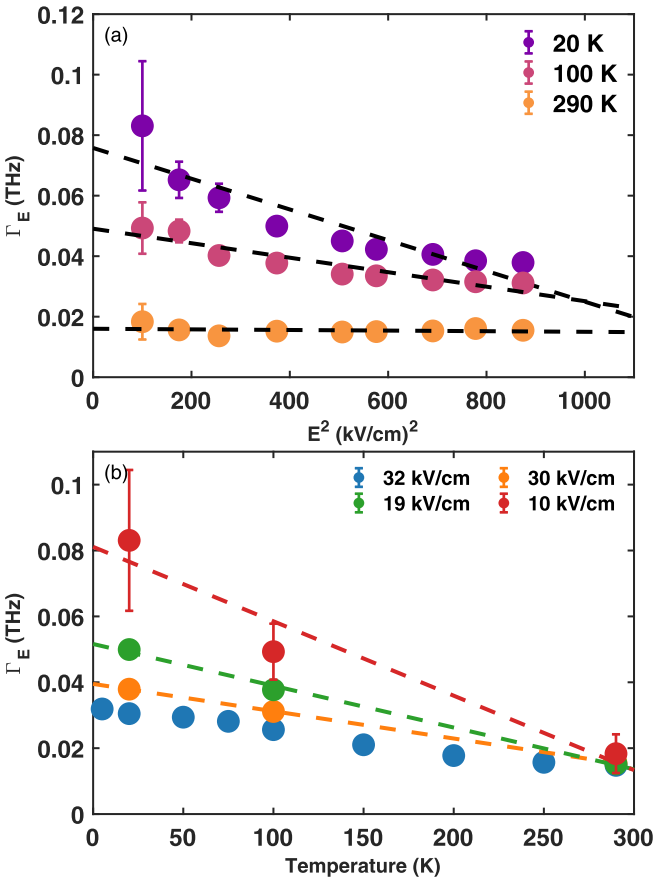

FIG. 4. Electronic energy relaxation rates as a function of fluence and temperature. (a) Energy relaxation rates for a single 100 nm thin film at different applied electric field strengths at three different fixed temperatures. The dashed lines are a guide to the eye. (b) Energy relaxation rates as a function of temperature at several fixed field strengths. The dashed lines are again a guide to the eye.

and lowest drive fields. This dependence of the rate on field is indicative of being out of the perturbative $\chi^{(3)}$ regime at the lowest temperatures. From the pump probe time traces, we can estimate that the induced change in conductivity at the highest fluence is of the same scale as the equilibrium conductivity itself, $\sim 1200^{-1}\text{cm}^{-1}$ consistent our observation of a nonperturbative response [61].

From 150 to 290 K, the measured energy relaxation rate is qualitatively consistent with conventional expectations. Γ_E does show the expected increasing dependence with decreasing temperature, but note that the dependence is far from $1/T$. Quite anomalously, the dependence is monotonic down to scales well below any reasonable estimate for this material's T_{BG}. In a conventional metal, T_{BG} is approximately the Debye temperature as $2k_F$ is of the order of a reciprocal lattice vector. The Debye temperature of Cd_3As_2 is estimated to be approximately 100 K via the specific heat [62] or 187 K via sound velocity [63]. These estimates of the Debye temperature can serve as a first estimate for the temperature range over which Γ_E is expected to increase with decreasing temperature. Of course, Cd_3As_2 is a semimetal and can—in principle—have a k_F that is much smaller than a reciprocal lattice vector. Taking our earlier estimate of the Fermi energy to be $\sim$0.2 eV, this corresponds to an estimated k_F of $\sim 0.08\,\text{Å}^{-1}$ under the modified Kane model for Cd_3As_2 [23,64]. This is 16% of the reciprocal lattice scale and so suggests the Fermi surface is not small enough to account for the discrepancy by itself. A far more likely source of the anomalies is that the phonon spectrum in Cd_3As_2 is found to be extremely non-Debye like. As mentioned, Cd_3As_2's unit cell is extremely large, incorporating 80 atoms in a unit cell. This leads to an unusually small Brillouin zone. Materials with small Brillouin zones tend to have anomalous phonons with many optical modes and low velocity acoustic ones [26]. In this regard, an examination of the specific heat [62] suggests the phonon spectrum is strongly non-Debye-like and has a number of anomalous and very soft low-frequency phonons that have also been observed in Raman [27]. Evidence for softening of phonon modes below 100 K due to the proximity of the Dirac semimetal state to a Kohn anomaly has been found in Raman scattering [27]. This softening leads to an increased phase space for phonon-phonon scattering and low phonon velocities and high damping. Irrespective of the origin, this reinforces the notion that the Debye temperature is not the relevant temperature scale to characterize the phonon spectrum in Cd_3As_2. Using a sound velocity of $\sim 2000\,\text{m s}^{-1}$ [63,65] and the k_F given above, one can estimate $T_{\text{BG}}/3$ to be $\sim$40 K, which is not so far from the lowest temperature we measure down to in Fig. 3(c). Nevertheless, the phonon spectrum is likely to be so non-Debye as to require explicit detailed calculations to find any agreement with experiment.

In the conventional theory of energy relaxation, coupling of low-energy acoustic phonons to electronic degrees of freedom are considered [46]. Of course, optical phonons can also serve as sinks for energy. In most materials, their energies are too high to be relevant to relaxation of a quasithermal distribution. However, in addition to anomalous acoustic phonons, Cd_3As_2 also has anomalous very low-energy optical phonons that could also carry off energy. Optical phonons are generally expected to give an exponentially activated form for Γ_E at low temperature and the same $1/T$ dependence at high temperature [60]. So, it is not even clear that their consideration would give greater understanding of the present data. Nevertheless, it would be interesting to do a detailed calculation using an experimentally determined phonon spectrum and calculate the energy relaxation rates, taking into account both acoustic and optical phonons.

In the conventional theory, the peak in Γ_E is found at a temperature above which the electron-phonon scattering is largely elastic. As no peak is found, the electron-phonon scattering can be inferred to be elastic for all measured temperatures and thus the Wiedemann-Franz law should be obeyed for the measured temperature ranges. Temperature-dependent elastic scattering is largely consistent with the fact that the current scattering rate is linear in T from the lowest measured T all the way up to 120 K. We note that with the previous measurements of the dimensionless electron-phonon coupling constant of $\lambda \approx 0.09$ (for optical phonons), the scattering rate in the elastic regime is predicted to be $2\pi\lambda k_B \text{T}/h \approx 0.56 k_B\ \text{T}/h$. Although this is much larger than the approximately $0.08 \pm 0.01\ k_B\text{T}/h$ found above, it is notable that the linear T dependence is found in this regime. The numeric discrepancy may be considered unsurprising due to

the extremely non-Debye character of the phonon spectrum and different phonon branches probed.

IV. CONCLUSION

In this paper, we have performed linear and nonlinear THz spectroscopy on the Dirac semimetal Cd_3As_2. We have found energy relaxation rates that are in magnitude far smaller then the momentum relaxation rates. The energy relaxation rate shows a temperature dependence qualitatively similar to that expected for a metal well above T_{BG}, but surprisingly exhibits this dependence to the lowest measured temperature, which are far lower than any conventional estimates for the Bloch-Grüneisen temperature. We find an electric field dependence that is consistent with this behavior and determine we are in a regime of temperature that gives an energy relaxation with an extremely low effective T_{BG}. This extremely low T_{BG} may stem from the low effective sound velocity induced by large number of optical phonon modes created by Cd_3As_2's large unit cell [26]. We believe the low effective T_{BG} corresponds to a regime of elastic electron-phonon scattering over the entire measured temperature range and also manifests itself in the linear-in-T dependence of the current dependent scattering rate that is observed up to 120 K. The nonlinear response we measure in the THz range is strongly nonperturbative, consistent with prior measurements. However, we find that the origin and scale of the nonlinear signal in Cd_3As_2 is directly connected to the heating and then subsequent relaxation of the electronic subsystem. We can observe this via the temperature and fluence dependence of our nonlinear response, which is enhanced as the heating of our electronic subsystem increases at lower temperature. This is substantiated by the lack of fluence dependence in our measured energy relaxation rates at room temperature, while at lower temperatures we observe strong dependence between pump fluence and relaxation rates.

The data that support the findings of this article are openly available at [66].

ACKNOWLEDGMENTS

Work at JHU and PSU was supported as part of the Institute for Quantum Matter, an Energy Frontier Research Center funded by the Office of Basic Energy Sciences of the Department of Energy, under Grant No. DE-SC0019331. Instrumentation development at JHU was supported by the Gordon and Betty Moore Foundation EPiQS Initiative Grant No. GBMF9454.

[1] T. O. Wehling, A. M. Black-Schaffer, and A. V. Balatsky, Dirac materials, Adv. Phys. **63**, 1 (2014).
[2] N. P. Armitage, E. J. Mele, and A. Vishwanath, Weyl and Dirac semimetals in three-dimensional solids, Rev. Mod. Phys. **90**, 015001 (2018).
[3] B. Q. Lv, T. Qian, and H. Ding, Experimental perspective on three-dimensional topological semimetals, Rev. Mod. Phys. **93**, 025002 (2021).
[4] T. Ando, T. Nakanishi, and R. Saito, Berry's phase and absence of back scattering in carbon nanotubes, J. Phys. Soc. Jpn. **67**, 2857 (1998).
[5] S. M. Young, S. Zaheer, J. C. Y. Teo, C. L. Kane, E. J. Mele, and A. M. Rappe, Dirac semimetal in three dimensions, Phys. Rev. Lett. **108**, 140405 (2012).
[6] Q. Wang, C.-Z. Li, S. Ge, J.-G. Li, W. Lu, J. Lai, X. Liu, J. Ma, D.-P. Yu, Z.-M. Liao, and D. Sun, Ultrafast broadband photodetectors based on three-dimensional dirac semimetal Cd_3As_2, Nano Lett. **17**, 834 (2017).
[7] H. T. Chorsi, S. Yue, P. P. Iyer, M. Goyal, T. Schumann, S. Stemmer, B. Liao, and J. A. Schuller, Widely tunable optical and thermal properties of dirac semimetal Cd_3As_2, Adv. Opt. Mater. **8**, 1901192 (2020).
[8] C. Rizza and A. Molle, Closing the THz gap with Dirac semimetals, Light Sci. Appl. **11**, 124 (2022).
[9] H. Da, Q. Song, P. Hu, and H. Ye, Prediction of negative refraction in Dirac semimetal metamaterial, Nanotechnology **33**, 415202 (2022).
[10] Y. Araki, T. Misawa, and K. Nomura, Long-range spin transport on the surface of topological Dirac semimetal, Phys. Rev. Res. **3**, 023219 (2021).
[11] S. Borisenko, Q. Gibson, D. Evtushinsky, V. Zabolotnyy, B. Büchner, and R. J. Cava, Experimental realization of a three-dimensional Dirac semimetal, Phys. Rev. Lett. **113**, 027603 (2014).
[12] Z. K. Liu, J. Jiang, B. Zhou, Z. J. Wang, Y. Zhang, H. M. Weng, D. Prabhakaran, S.-K. Mo, H. Peng, P. Dudin, T. Kim, M. Hoesch, Z. Fang, X. Dai, Z. X. Shen, D. L. Feng, Z. Hussain, and Y. L. Chen, A stable three-dimensional topological Dirac semimetal Cd_3As_2, Nat. Mater. **13**, 677 (2014).
[13] M. N. Ali, Q. Gibson, S. Jeon, B. B. Zhou, A. Yazdani, and R. J. Cava, The crystal and electronic structures of Cd_3As_2, the three-dimensional electronic analogue of graphene, Inorg. Chem. **53**, 4062 (2014).
[14] H. Kim, M. Goyal, S. Salmani-Rezaie, T. Schumann, T. N. Pardue, J.-M. Zuo, and S. Stemmer, Point group symmetry of cadmium arsenide thin films determined by convergent beam electron diffraction, Phys. Rev. Mater. **3**, 084202 (2019).
[15] A. J. Rosenberg and T. C. Harman, Cd_3As_2 —a noncubic semiconductor with unusually high electron mobility, J. Appl. Phys. **30**, 1621 (1959).
[16] T. Liang, Q. Gibson, M. N. Ali, M. Liu, R. J. Cava, and N. P. Ong, Ultrahigh mobility and giant magnetoresistance in the Dirac semimetal Cd_3As_2, Nat. Mater. **14**, 280 (2015).
[17] A. Akrap, M. Hakl, S. Tchoumakov, I. Crassee, J. Kuba, M. O. Goerbig, C. C. Homes, O. Caha, J. Novák, F. Teppe, W. Desrat, S. Koohpayeh, L. Wu, N. P. Armitage, A. Nateprov, E. Arushanov, Q. D. Gibson, R. J. Cava, D. van der Marel, B. A. Piot *et al.*, Magneto-optical signature of massless Kane electrons in Cd_2As_3, Phys. Rev. Lett. **117**, 136401 (2016).
[18] C. M. Wang, H.-Z. Lu, and S.-Q. Shen, Anomalous phase shift of quantum oscillations in 3D topological semimetals, Phys. Rev. Lett. **117**, 077201 (2016).

[19] M. Uchida, Y. Nakazawa, S. Nishihaya, K. Akiba, M. Kriener, Y. Kozuka, A. Miyake, Y. Taguchi, M. Tokunaga, N. Nagaosa, Y. Tokura, and M. Kawasaki, Quantum Hall states observed in thin films of Dirac semimetal Cd_3As_2, Nat. Commun. **8**, 2274 (2017).

[20] T. Schumann, L. Galletti, D. A. Kealhofer, H. Kim, M. Goyal, and S. Stemmer, Observation of the quantum Hall effect in confined films of the three-dimensional Dirac semimetal Cd_3As_2, Phys. Rev. Lett. **120**, 016801 (2018).

[21] M. Goyal, L. Galletti, S. Salmani-Rezaie, T. Schumann, D. A. Kealhofer, and S. Stemmer, Thickness dependence of the quantum Hall effect in films of the three-dimensional Dirac semimetal Cd_3As_2, APL Mater. **6**, 026105 (2018).

[22] L. Galletti, T. Schumann, D. A. Kealhofer, M. Goyal, and S. Stemmer, Absence of signatures of Weyl orbits in the thickness dependence of quantum transport in cadmium arsenide, Phys. Rev. B **99**, 201401(R) (2019).

[23] B. Cheng, T. Schumann, S. Stemmer, and N. P. Armitage, Probing charge pumping and relaxation of the chiral anomaly in a Dirac semimetal, Sci. Adv. **7**, eabg0914 (2021).

[24] R. Xiao, J. Zhang, J. Chamorro, J. Kim, T. M. McQueen, D. Vanderbilt, M. Kayyalha, Y. Li, and N. Samarth, Integer quantum Hall effect and enhanced *g* factor in quantum-confined Cd_3As_2Films, Phys. Rev. B **106**, L201101 (2022).

[25] H. Li, H. He, H.-Z. Lu, H. Zhang, H. Liu, R. Ma, Z. Fan, S.-Q. Shen, and J. Wang, Negative magnetoresistance in Dirac semimetal Cd_3As_2, Nat. Commun. **7**, 10301 (2016).

[26] Z. Chen, X. Zhang, and Y. Pei, Manipulation of phonon transport in thermoelectrics, Adv. Mater. **30**, 1705617 (2018).

[27] S. Yue, H. T. Chorsi, M. Goyal, T. Schumann, R. Yang, T. Xu, B. Deng, S. Stemmer, J. A. Schuller, and B. Liao, Soft phonons and ultralow lattice thermal conductivity in the Dirac semimetal Cd_3As_2, Phys. Rev. Res. **1**, 033101 (2019).

[28] D. P. Spitzer, G. A. Castellion, and G. Haacke, Anomalous thermal conductivity of Cd_3As_2 and the Cd_3As_2-Zn_3As_2 Alloys, J. Appl. Phys. **37**, 3795 (1966).

[29] H. Wang, X. Luo, W. Chen, N. Wang, B. Lei, F. Meng, C. Shang, L. Ma, T. Wu, X. Dai, Z. Wang, and X. Chen, Magnetic-field enhanced high-thermoelectric performance in topological Dirac semimetal Cd_3As_2 crystal, Sci. Bull. **63**, 411 (2018).

[30] D. Barbalas, R. Romero III, D. Chaudhuri, F. Mahmood, H. P. Nair, N. J. Schreiber, D. G. Schlom, K. M. Shen, and N. P. Armitage, Energy Relaxation and dynamics in the correlated metal Sr_2RuO_4 via THz two-dimensional coherent spectroscopy, arXiv:2312.13502.

[31] M. C. Hoffmann, J. Hebling, H. Y. Hwang, K.-L. Yeh, and K. A. Nelson, THz-pump/THz-probe spectroscopy of semiconductors at high field strengths [Invited], J. Opt. Soc. Am. B **26**, A29 (2009).

[32] J. Hebling, M. C. Hoffmann, H. Y. Hwang, K.-L. Yeh, and K. A. Nelson, Observation of nonequilibrium carrier distribution in Ge, Si, and GaAs by terahertz pump–terahertz probe measurements, Phys. Rev. B **81**, 035201 (2010).

[33] R. H. M. Groeneveld, R. Sprik, and A. Lagendijk, Femtosecond spectroscopy of electron-electron and electron-phonon energy relaxation in Ag and Au, Phys. Rev. B **51**, 11433 (1995).

[34] V. V. Kabanov and A. S. Alexandrov, Electron relaxation in metals: Theory and exact analytical solutions, Phys. Rev. B **78**, 174514 (2008).

[35] V. V. Kabanov, Electron-electron and electron-phonon relaxation in metals excited by optical pulse, Low Temp. Phys. **46**, 414 (2020).

[36] C. P. Weber, B. S. Berggren, M. G. Masten, T. C. Ogloza, S. Deckoff-Jones, J. Madéo, M. K. L. Man, K. M. Dani, L. Zhao, G. Chen, J. Liu, Z. Mao, L. M. Schoop, B. V. Lotsch, S. S. P. Parkin, and M. Ali, Similar ultrafast dynamics of several dissimilar Dirac and Weyl semimetals, J. Appl. Phys. **122**, 223102 (2017).

[37] W. Lu, S. Ge, X. Liu, H. Lu, C. Li, J. Lai, C. Zhao, Z. Liao, S. Jia, and D. Sun, Ultrafast relaxation dynamics of photoexcited Dirac fermions in the three-dimensional Dirac semimetal Cd_3As_2, Phys. Rev. B **95**, 024303 (2017).

[38] C. Zhu, X. Yuan, F. Xiu, C. Zhang, Y. Xu, R. Zhang, Y. Shi, and F. Wang, Broadband hot-carrier dynamics in three-dimensional Dirac semimetal Cd_3As_2, Appl. Phys. Lett. **111**, 091101 (2017).

[39] W. Lu, J. Ling, F. Xiu, and D. Sun, Terahertz probe of photoexcited carrier dynamics in the Dirac semimetal Cd_2As_3, Phys. Rev. B **98**, 104310 (2018).

[40] W. Zhang, Y. Yang, P. Suo, W. Zhao, J. Guo, Q. Lu, X. Lin, Z. Jin, L. Wang, G. Chen, F. Xiu, W. Liu, C. Zhang, and G. Ma, Ultrafast photocarrier dynamics in a 3D Dirac semimetal Cd_3As_2 film studied with terahertz spectroscopy, Appl. Phys. Lett. **114**, 221102 (2019).

[41] C. Reinhoffer, Y. Mukai, S. Germanskiy, A. Bliesener, G. Lippertz, A. Uday, A. A. Taskin, Y. Ando, Z. Wang, and P. H. M. van Loosdrecht, Relaxation dynamics of the optically driven nonequilibrium states in the electron- and hole-doped topological-insulator materials $(Bi_{x-1}Sb_x)Te_3$, Phys. Rev. Mater. **4**, 124201 (2020).

[42] G. Zhai, C. Ma, J. Xiang, J. Ye, T. Li, Y. Li, P. Sun, G. Chen, X. Wu, and X. Zhang, Mid-infrared transient reflectance study of the Dirac semimetal Cd_3As_2 under strong optical pumping, Phys. Rev. B **101**, 174310 (2020).

[43] C. Bao, Q. Li, S. Xu, S. Zhou, X.-Y. Zeng, H. Zhong, Q. Gao, L. Luo, D. Sun, T.-L. Xia, and S. Zhou, Population inversion and Dirac fermion cooling in 3D Dirac semimetal Cd_3As_2, Nano Lett. **22**, 1138 (2022).

[44] B. Cheng, N. Kanda, T. N. Ikeda, T. Matsuda, P. Xia, T. Schumann, S. Stemmer, J. Itatani, N. P. Armitage, and R. Matsunaga, Efficient terahertz harmonic generation with coherent acceleration of electrons in the Dirac semimetal Cd_3As_2, Phys. Rev. Lett. **124**, 117402 (2020).

[45] S. Kovalev, R. M. A. Dantas, S. Germanskiy, J.-C. Deinert, B. Green, I. Ilyakov, N. Awari, M. Chen, M. Bawatna, J. Ling, F. Xiu, P. H. M. van Loosdrecht, P. Surówka, T. Oka, and Z. Wang, Non-perturbative terahertz high-harmonic generation in the three-dimensional Dirac semimetal Cd_3As_2, Nat. Commun. **11**, 2451 (2020).

[46] P. B. Allen, Theory of thermal relaxation of electrons in metals, Phys. Rev. Lett. **59**, 1460 (1987).

[47] C. Zhang, T. Zhou, S. Liang, J. Cao, X. Yuan, Y. Liu, Y. Shen, Q. Wang, J. Zhao, Z. Yang, and F. Xiu, Unexpected low thermal conductivity and large power factor in Dirac semimetal Cd_3As_2, Chin. Phys. B **25**, 017202 (2016).

[48] K. Bartkowski, G. Pompe, and E. Hegenbarth, Specific heat of single-crystalline Cd_3As_2, Cd_3P_2, and at low temperatures, Physica Stat. Sol. (a) **111**, K165 (1989).

[49] A. Lavasani, D. Bulmash, and S. Das Sarma, Wiedemann-Franz law and Fermi liquids, Phys. Rev. B **99**, 085104 (2019).

[50] W. Yanez, Y. Ou, R. Xiao, J. Koo, J. T. Held, S. Ghosh, J. Rable, T. Pillsbury, E. G. Delgado, K. Yang, J. Chamorro, A. J. Grutter, P. Quarterman, A. Richardella, A. Sengupta, T. McQueen, J. A. Borchers, K. A. Mkhoyan, B. Yan, and N. Samarth, Spin and charge interconversion in Dirac semimetal thin films, Phys. Rev. Appl. **16**, 054031 (2021).

[51] F. Mahmood, D. Chaudhuri, S. Gopalakrishnan, R. Nandkishore, and N. P. Armitage, Observation of a marginal Fermi glass, Nat. Phys. **17**, 627 (2021).

[52] M. Woerner, W. Kuehn, P. Bowlan, K. Reimann, and T. Elsaesser, Ultrafast two-dimensional terahertz spectroscopy of elementary excitations in solids, New J. Phys. **15**, 025039 (2013).

[53] B. Cheng, T. Schumann, Y. Wang, X. Zhang, D. Barbalas, S. Stemmer, and N. P. Armitage, A large effective phonon magnetic moment in a Dirac semimetal, Nano Lett. **20**, 5991 (2020).

[54] A. Damascelli, Optical spectroscopy of quantum spin systems, Ph.D. thesis, University of Groningen, Groningen, Netherlands, 1999.

[55] C. C. Homes, Y. M. Dai, A. Akrap, S. L. Bud'ko, and P. C. Canfield, Vibrational anomalies in AFe_2As_2(A = Ca, Sr, and Ba) single crystals, Phys. Rev. B **98**, 035103 (2018).

[56] P. E. C. Ashby and J. P. Carbotte, Chiral anomaly and optical absorption in Weyl semimetals, Phys. Rev. B **89**, 245121 (2014).

[57] M. Conforti and G. Della Valle, Derivation of third-order nonlinear susceptibility of thin metal films as a delayed optical response, Phys. Rev. B **85**, 245423 (2012).

[58] K. Katsumi, J. Fiore, M. Udina, R. Romero, III, D. Barbalas, J. Jesudasan, P. Raychaudhuri, G. Seibold, L. Benfatto, and N. P. Armitage, Revealing novel aspects of light-matter coupling in terahertz two-dimensional coherent spectroscopy: The case of the amplitude mode in superconductors, Phys. Rev. Lett. **132**, 256903 (2024).

[59] D. Wu, X. Wang, X. Zhang, C. Yang, P. Zheng, P. Li, and Y. Shi, Large and anisotropic linear magnetoresistance in bulk stoichiometric Cd_3As_2 crystals, Sci. China Phys. Mech. Astron. **58**, 1 (2015).

[60] P. Glorioso and S. A. Hartnoll, Joule heating in bad and slow metals, SciPost Physics **13**, 095 (2022).

[61] These estimates were obtained with the expression $\Delta\sigma(\tau) \approx \frac{n_{\text{sub}}+1}{dZ_0T}\left(\frac{-E_{\text{NL}}(\tau)}{E_{AB}(\tau)-E_A}(\tau)\right)$.

[62] A. de Combarieu and J. P. Jay-Gerin, Specific heat of cadmium arsenide (Cd_2As_3) below 30 K, Phys. Rev. B **25**, 2923 (1982).

[63] Z. Wang, H. Zhao, M. Lyu, J. Xiang, Q. Dong, G. Chen, S. Zhang, and P. Sun, Unusual thermodynamics of low-energy phonons in the Dirac semimetal Cd_3As_2, Chin. Phys. B **31**, 106501 (2022).

[64] Z. Wang, H. Weng, Q. Wu, X. Dai, and Z. Fang, Three-dimensional Dirac semimetal and quantum transport in Cd_2As_3, Phys. Rev. B **88**, 125427 (2013).

[65] G. Liang, G. Zhai, J. Ma, H. Wang, J. Zhao, X. Wu, and X. Zhang, Ultrafast optical probe of coherent acoustic phonons in Dirac semimetal Cd_3As_2 film epitaxied on GaAs(111)B substrate, J. Phys. Chem. Lett. **13**, 8783 (2022).

[66] https://zenodo.org/records/12523686.